nature physics

SUPPLEMENTARY INFORMATION

DOI: 10.1038/NPHYS3826

Physical realization of a quantum spin liquid based on a complex frustration mechanism

Christian Balz,[1,2,*] Bella Lake,[1,2] Johannes Reuther,[1,3] Hubertus Luetkens,[4] Rico Schönemann,[5] Thomas Herrmannsdörfer,[5] Yogesh Singh,[6] A.T.M. Nazmul Islam,[1] Elisa M. Wheeler,[7] Jose A. Rodriguez-Rivera,[8,9] Tatiana Guidi,[10] Giovanna G. Simeoni,[11] Chris Baines,[4] and Hanjo Ryll[1]

[1] *Helmholtz-Zentrum Berlin für Materialien und Energie, 14109 Berlin, Germany*
[2] *Institut für Festkörperphysik, Technische Universität Berlin, 10623 Berlin, Germany*
[3] *Dahlem Center for Complex Quantum Systems and Fachbereich Physik, Freie Universität Berlin, 14195 Berlin, Germany*
[4] *Laboratory for Muon-Spin Spectroscopy, Paul Scherrer Institut, 5232 Villigen, Switzerland*
[5] *Hochfeld-Magnetlabor Dresden (HLD-EMFL), Helmholtz-Zentrum Dresden-Rossendorf, 01314 Dresden, Germany*
[6] *Indian Institute of Science Education and Research (IISER) Mohali, Knowledge City, Sector 81, Mohali 140306, India*
[7] *Institut Laue-Langevin, 38042 Grenoble, France*
[8] *NIST Center for Neutron Research, National Institute of Standards and Technology, 20899 Gaithersburg, USA*
[9] *Department of Materials Science, University of Maryland, College Park, 20742 Maryland, USA*
[10] *ISIS Facility, STFC Rutherford Appleton Laboratory, Oxfordshire OX11 0QX, UK*
[11] *Heinz Maier-Leibnitz Zentrum, Technische Universitat München, 85748 Garching, Germany*

(Dated: June 10, 2016)

I. CRYSTAL STRUCTURE

The crystal structure of $Ca_{10}Cr_7O_{28}$ given in table **1** has been refined from X-ray synchrotron powder diffraction at 300 K and is in agreement with literature [1, 2]. Additional neutron single crystal diffraction with higher sensitivity for the Oxygen atoms confirms the structure and neutron powder diffraction performed between 300 K and 2 K shows that the structure remains unchanged in this temperature range. There are three inequivalent Cr ions in the structure, Cr1 and Cr2 occupy Wyckoff site $18b1$, they form the kagome bilayer structure and are represented by black and gray spheres in figure **1** of the main text, Cr3 occupies the $6a3$ site and lies close to the centers of the hexagonal hole in the kagome bilayers (not shown). Performing a valance bond sum calculation using the tabulated BVS constants for Chromium from Brown *et al.* [3] shows that Cr1 and Cr2 have valance 5+ while Cr3 has valance 6+ as given in table **2**. The Cr^{5+} ions have spin-½ and are important for the magnetism while Cr^{6+} is non-magnetic. All Cr ions are surrounded by distorted Oxygen tetrahedra (table **2**). The resulting strong and distorted crystal field quenches the orbital angular momentum resulting in spin-only magnetic moments typical for transition metals.

The Rietveld refinement of the diffraction data places the upper limit of site mixing between Ca and Cr sites at 1.5%. However site mixing is not expected in $Ca_{10}Cr_7O_{28}$ since the Ca^{2+} and Cr^{5+}/Cr^{6+} ions have very different valences and the ratio of their atomic radii is large. Taking the radii from Shannon *et al.* [4] one obtains average radii for Ca of 1.06Å and for Cr of 0.345Å. The ratio of 1.06/0.345 is rather large compared to e.g. the ratio of the radii of Yb^{3+} to Ti^{4+} in $Yb_2Ti_2O_7$ being 0.985/0.605.

II. MAGNETIC PROPERTIES

The absence of any phase transition as well as the spin only magnetic moment mentioned in the main text are further verified by magnetization measurements. The DC susceptibility data (Fig. **1a**) reveals only smoothly varying features down to 2 K. It also provides further evidence for the spin-1/2 magnetic moment of Cr1 and Cr2 and the non-magnetic nature of the Cr3 ions. By fitting the inverse susceptibility to a Curie-Weiss law in the temperature range 50-250 K the effective moment per Cr ion yields 6/7·1.74(2) μ_B (1.73 μ_B is the effective moment for spin-1/2 and g=2) suggesting that only 6 of 7 Cr ions are magnetic. Our magnetization measurements (Fig. **1b**) also support this spin value because at a field of 12 T the magnetization saturates at a value of 6/7 μ_B as expected if 1 in 7 Cr ions is non-magnetic while the remaining 6 Cr ions have spin-1/2 and a g-factor of 2. This is indeed the number ratio of Cr3 to Cr1 and Cr2 in the crystal structure. An earlier XANES measurement [5] of $Ca_{10}Cr_7O_{28}$ detected an average Cr valence of 5.3(1) which is close to the average valence 5.14 for a ratio of 6:1 among the 5+ and the 6+ Cr ions.

The saturation value of 12 T of the magnetization curve further confirms the magnetic energy scale of $Ca_{10}Cr_7O_{28}$. The saturation field is equivalent to an energy of 1.4 meV for spin-1/2 moments which is comparable to the maximum energy of the magnetic excitations observed in a powder sample of $Ca_{10}Cr_7O_{28}$ (see figure **4a** of the main text). From the fit of the susceptibility to the Curie-Weiss law in the paramagnetic regime a Curie-Weiss temperature of 2.35 K could be extracted.

* christian.balz@helmholtz-berlin.de

DOI: 10.1038/NPHYS3826

Table 1. **Crystal structure.** Lattice parameters, atomic positions and Cr-Cr bond distances of $Ca_{10}Cr_7O_{28}$ from the crystal structure refinement at 300 K. The refinement was carried out in the tetragonal space group $R3c$ using X-ray synchrotron powder data. The occupancies for the partly filled non-magnetic Cr^{6+} positions were refined to 0.726(12) for Cr3A and 0.276(12) for Cr3B. The same ratio applies to O3A and O3B.

Lattice Parameters		Space Group		
a	10.76892(3) Å	$R3c$		
c	38.09646(12) Å			
Atom	x	y	z	B_{iso}[Å^2]
Ca1	0.28548(17)	0.15745(16)	-0.05744(3)	1.661(38)
Ca2	0.19737(17)	-0.19624(18)	0.00371(0)	0.754(18)
Ca3	0.38806(16)	0.18233(17)	0.03747(2)	0.754(18)
Ca4	2/3	1/3	0.10343(7)	0.794(42)
Cr1	0.31133(19)	0.14053(21)	0.13588(4)	0.564(12)
Cr2	0.17771(18)	-0.13669(19)	-0.09600(4)	0.564(12)
Cr3A	0	0	0.00446(10)	0.564(12)
Cr3B	0	0	0.02961(23)	0.564(12)
O3A	0	0	-0.03863(9)	2.254(55)
O3B	0	0	0.07192(26)	2.254(55)
O1	0.28286(18)	0.08966(16)	0.09384(3)	2.254(55)
O2	0.23570(17)	0.23520(18)	0.14947(3)	2.254(55)
O3	0.27626(12)	-0.01602(12)	0.15721(3)	0.872(49)
O4	0.49099(14)	0.24584(15)	0.14533(3)	0.872(49)
O5	0.14995(20)	-0.12682(19)	-0.05274(3)	2.254(55)
O6	0.25594(15)	-0.23730(15)	-0.10634(4)	0.872(49)
O7	0.29992(15)	0.03281(12)	-0.10850(4)	0.872(49)
O8	0.01423(15)	-0.22258(1)	-0.11430(4)	2.254(55)
O9	-0.00401(22)	0.14481(14)	0.01693(5)	2.254(55)
Bond	Distance [Å]	Bond	Distance [Å]	
J0	3.883			
J11	4.103	J12	4.167	
J21	5.033	J22	5.095	
J31	5.697	J32	5.724	

Table 2. **CrO_4 tetrahedra.** Cr-O distances for the two magnetic Cr ions and bond valence sum calculation for all four Cr ions.

Bond	Distance [Å]		Bond	Distance [Å]	
Cr1-O1	1.6695		Cr2-O5	1.6871	
Cr1-O2	1.6743		Cr2-O6	1.6991	
Cr1-O3	1.7343		Cr2-O7	1.6760	
Cr1-O4	1.7229		Cr2-O8	1.7170	
Ion	BVS	nominal	Ion	BVS	nominal
Cr1	4.85+	5+	Cr3A	5.89+	6+
Cr2	4.90+	5+	Cr3B	6.00+	6+

This is only compatible with the magnetic energy scale in $Ca_{10}Cr_7O_{28}$ of ∼16.2 K (1.4 meV) by assuming a mixture of FM and AFM interactions. A positive Curie-Weiss temperature also indicates a dominance of FM interactions in this material. Furthermore from the DC susceptibility data of $Ca_{10}Cr_7O_{28}$ no magnetic anisotropy is visible, the susceptibility appears to be independent of the field direction indicating Heisenberg interactions.

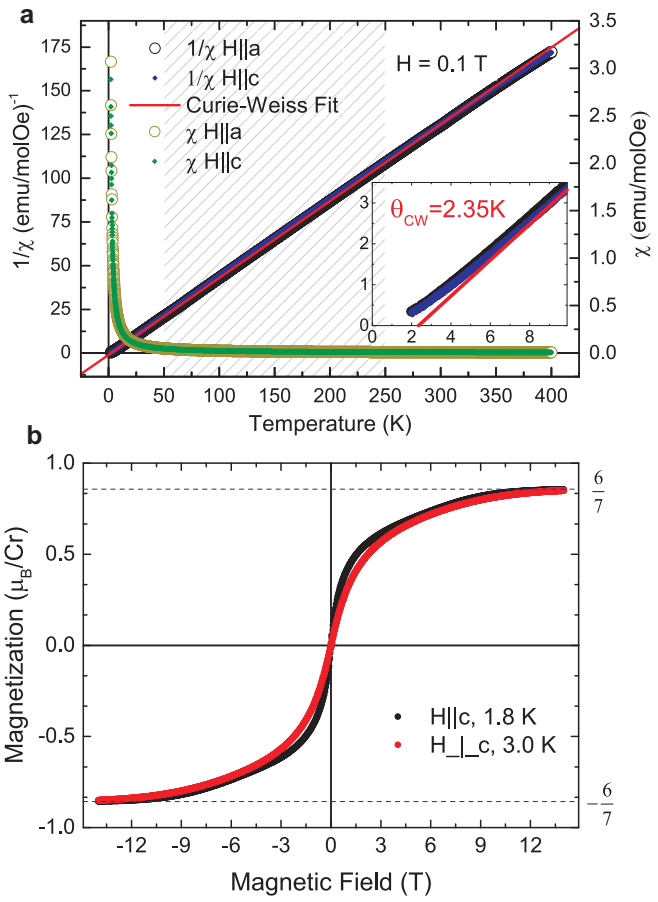

Figure 1. **Magnetization data. a**, Susceptibility measured at 0.1 T applied parallel to the a and c axis. The inverse susceptibility is overplotted. The red line is a fit to the Curie-Weiss law for $H||a$ in the temperature region indicated by the shading. The inset shows deviations from Curie-Weiss behavior at low temperatures. **b**, Magnetization at 1.8 K (3 K) as a function of magnetic field applied parallel to the c axis (perpendicular to the c axis).

III. ADDITIONAL INELASTIC NEUTRON SCATTERING DATA

Additional inelastic neutron scattering data to further demonstrate the two-dimensionality of the magnetic interactions in $Ca_{10}Cr_7O_{28}$ is shown in figure **2**. As described in more detail below, a sufficiently large external magnetic field aligns the spins ferromagnetically destroying the diffuse scattering and creates spin-wave excitations in $Ca_{10}Cr_7O_{28}$ which can be observed via inelastic neutron scattering. An interaction between magnetic ions is now visible as a dispersion of the spin wave modes in the direction of the interaction. This is observed easily since spin waves are sharp in energy. Inelastic neutron scattering measured at 9 T where the spins are close to saturation is shown in figure **2**. Dispersive spin wave modes are clearly visible in figure **2**(left) where the energy transfer is plotted versus the $[h, h, 0]$

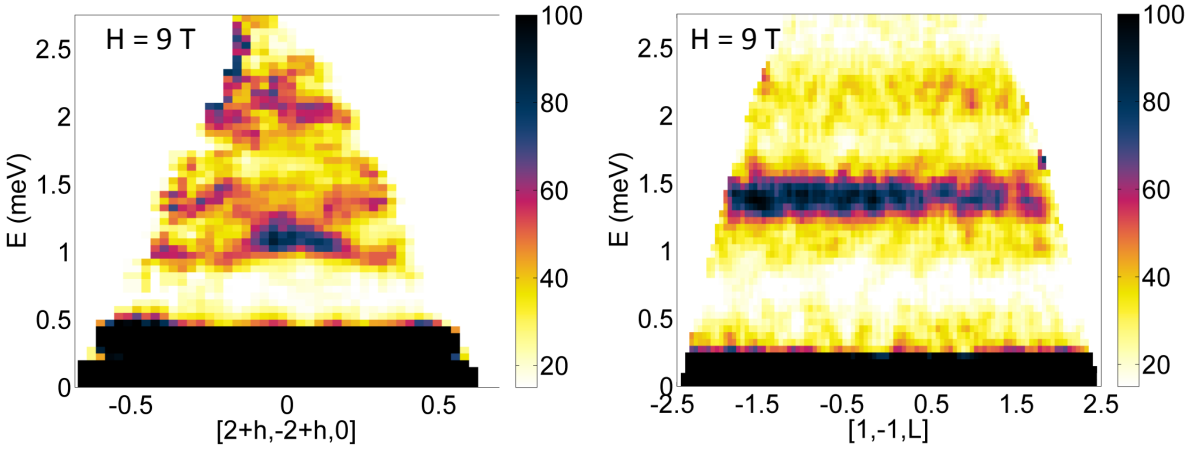

Figure 2. **Single crystal inelastic neutron scattering data under external magnetic field.** Inelastic neutron scattering along the $[h,h,0]$ and $[0,0,L]$ directions at 9 T and 2 K measured using the LET spectrometer at the ISIS facility, Rutherford Appleton Laboratory, U.K.. The slice along $[h,h,0]$ is integrated along the perpendicular $[k,-k,0]$ direction in the range $1.75 < k < 2.25$ and along $[0,0,L]$ between $-2.5 < L < 2.5$. The slice along $[0,0,L]$ is integrated over the perpendicular directions $[h,h,0]$ and $[k,-k,0]$ between $0.75 < h,k < 1.25$.

reciprocal space direction in the kagome plane (this corresponds to the direction shown in figure **4b** of the main text). In contrast to this, the spin wave mode along the out-of-plane $[0,0,L]$ direction lacks dispersion completely indicating the absence of continuous magnetic interactions in this direction. Therefore the magnetic coupling in $Ca_{10}Cr_7O_{28}$ is restricted to the $[h,k,0]$ kagome plane. This is an important constraint for the magnetic Hamiltonian of $Ca_{10}Cr_7O_{28}$ whose derivation will be describe in the following section.

IV. THE HAMILTONIAN

A lot of information about the magnetic Hamiltonian can be extracted from the diffraction and bulk properties measurements. From the crystal structure refinement it is clear that the CrO_4 tetrahedra are always distorted leading to quenched orbital moments. This in turn yields spin-only moments and Heisenberg interactions. The DC susceptibility data confirms that the interactions are isotropic (Heisenberg) since no difference between the in-plane and out-of-plane field directions was observed (see Fig. **1a**). Furthermore, the small Curie-Weiss temperature of 2.35 K reveals that $Ca_{10}Cr_7O_{28}$ features a mixture of ferromagnetic and antiferromagnetic interactions. The magnetization measurement reveals saturation at 12 T suggesting the magnetic excitations do not extend beyond 1.4 meV, therefore no individual exchange interactions is expected to be greater than 1.4 meV. Finally, in agreement with the specific heat (Fig. **2b** of the main text), there is no indication of an energy gap between the ground state and first excited state which excludes dimerization due to a single dominant antiferromagnetic interaction. The most important result of the magnetization measurement is however that a magnetic field of 12 T is sufficient to overcome the interactions and align the spins in the direction of the external field. This creates a ferromagnetic ground state and induces spin-wave excitations which can be measured using inelastic neutron scattering. The aim would be to fit the excitations to linear spin-wave theory and extract the exchange interactions using the method described in Refs. [6, 7].

Figure **3** shows the inelastic neutron scattering data collected at 11 T. Gapped dispersive excitations are clearly visible along the $[h,-h,0]$ and $[2+h,-2+h,0]$ directions in the plane of the kagome bilayers. For the spin wave fitting the dispersions were extracted from the 2D data using constant-Q cuts along both directions in steps of 0.1 r.l.u. while the stepsize in energy was 0.1 meV between 1 and 2.4 meV and 0.2 meV above. A total of 40 cuts were fitted to extract the energy and intensity of the spin-wave modes.

The appropriate Heisenberg Hamiltonian under external magnetic field considering only nearest-neighbor exchange interactions takes the form

$$\mathcal{H} = \sum_{i,j} \boldsymbol{S}_i J_{ij} \boldsymbol{S}_j + \boldsymbol{B} \sum_i g \boldsymbol{S}_i \qquad (1)$$

where $\boldsymbol{S}_i$ are spin vector operators, $J_{i,j}$ are matrices describing the pair coupling between spins, $\boldsymbol{B}$ is the external magnetic field and g is the g-factor. The possible inequivalent nearest-neighbor exchange interactions were identified from the crystal structure (see Fig. **1a** of the main text) which yielded seven Cr-Cr couplings within realistic bond distances. Further the magnetic structure at this field was assumed to be ferromagnetic with all spins aligned along the field direction. With this information

DOI: 10.1038/NPHYS3826

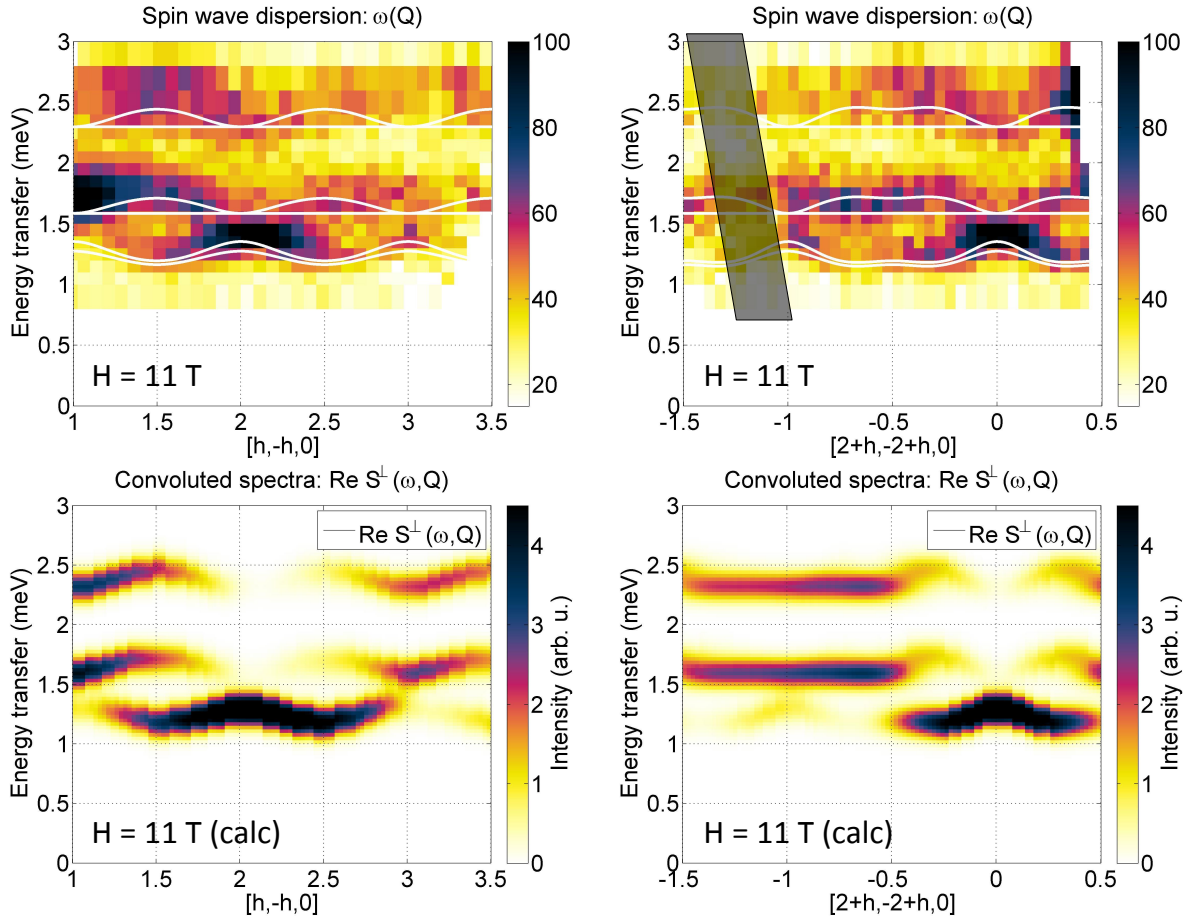

Figure 3. **Single crystal inelastic neutron scattering data under external magnetic field and linear spin wave theory.** (first row) Inelastic neutron scattering along the $[h,-h,0]$ and $[h,h,0]$ directions at 11 T and 90 mK measured using the MACS spectrometer. The shaded region in the top right panel has lower intensity due to attenuation by the supporting structures in the magnet. This region is not fitted. The data are integrated along the perpendicular directions in the range of ± 0.1 r.l.u.. The spin wave modes obtained from linear spin wave theory are overplotted. (second row) Intensity distribution calculated from linear spin wave theory using the best fit parameters given in (2) and an external magnetic field of 11 T. The calculated $S(\mathbf{Q},\omega)$ is convolved with a Gaussian of FWHM 0.4 meV for realistic comparison to the data.

a Hamiltonian according to (1) was generated with random starting parameters which were fitted to the spin-wave spectra using a non-linear least square minimization routine. For this purpose the spin-spin correlation function was calculated from the Hamiltonian and compared to the energy and the intensity of the spin wave modes determined experimentally using the SpinW Matlab routine [8]. To generate the random starting parameters the constraints obtained from the bulk properties as well as from the INS measurements described above were used. The best fit obtained in this manner corresponds to the exchange couplings

$$\begin{aligned} J0 &= -0.08(4)\ meV, \quad J11 = 0, \quad J21 = 0, \\ J21 &= -0.76(5)\ meV, \quad J22 = -0.27(3)\ meV, \\ J31 &= 0.09(2)\ meV, \quad J32 = 0.11(3)\ meV. \end{aligned} \tag{2}$$

Uncertainties were determined by visual comparison of the theoretical and experimental inelastic structure factors. In this way the dispersion relation was fitted to the data while the overall intensity of the calculated spin wave modes was scaled to agree with the experimental intensity at the highest intensity point found at [2,-2,0] and E=1.4meV. The resulting $S(\mathbf{Q},\omega)$ is shown alongside the 11 T data in figure **3**. Finally simulations along other reciprocal space directions were performed and compared to the corresponding slices through the data as an addition check. It is clear that the extracted parameters correctly reproduce the observed spin-wave energies and intensities at most wavevectors. A few small mismatches indicate that further investigation may be necessary to refine the Hamiltonian. These parameters lead to the kagome bilayer model where $J11$ and $J12$ are set to zero to satisfy the constrain of no continuous magnetic coupling along the L direction. Magnetic models where $J0$ is zero while $J11$ and $J12$ are finite or even all three out-of-plane interactions ($J0$, $J11$ and $J12$) are zero could not produce fits of similar accuracy.

The spectra in the hk0 plane of figure **3** have very rich features. There are dispersive as well as flat bands visible. It is not straightforward to track which features are due to which terms in the Hamiltonian but a few trends can be observed. The energy of the lowest band only depends on J0 while the energies of the 2nd and 3rd band mainly depend on J22 and J21 respectively. The amplitude of the dispersion is influenced by J31 and J32 where stronger antiferromagnetic couplings correspond to an increased dispersion.

The exchange parameters obtained in the high-field phase can be used to suggest the effective classical ground state of $Ca_{10}Cr_7O_{28}$ by simply putting the magnetic field term to zero in the Hamiltonian. Then the energy of the ground state can be minimized using mean-field theory with the restriction to single-k magnetic structures. The result is the classical zero-field ground state for this Hamiltonian and the characteristic spin arrangement is given in figure **1e** of the main text. In the real ground state this spin arrangement is however exposed to strong fluctuations as shown by the absence of any experimental evidence for a zero-field transition to long-range magnetic order. Nevertheless this provides a snapshot of the correlations in the real system, showing approximately ferromagnetic alignment of the spins on the ferromagnetic triangles (green triangles) and a distorted 120° alignment on the antiferromagnetic triangles (blue triangles).

V. PFFRG APPROACH AND THE STABILITY OF THE QUANTUM DISORDERED PHASE

A. Implementation of the PFFRG

As explained in equation (2) in the main text the PFFRG approach uses the pseudofermion description of spin operators. The advantage of this representation is that a fermionic model can be treated using standard Feynman many-body techniques. Since spin models are inherently strongly coupled quantum systems without a small parameter, diagrammatic summations need to be performed in infinite order in J which is accomplished by the FRG approach. This technique first introduces an artificial infrared frequency cutoff Λ in the fermionic Green's function which suppresses the fermion propagation below the energy Λ. The FRG then formulates an infinite hierarchy of coupled differential equations for the evolution of all m-particle vertex functions under the flow of Λ. In order to obtain a closed set of equations that can be solved numerically, a truncation scheme needs to be applied. Here we use the Katanin trunation which has proven to be appropriate for the description of strongly correlated spin systems [9, 10]. This scheme neglects all three-particle vertices expect for those which can be written as a self-energy insertion in the two-particle vertex. This ensures a complete backfeeding of the self-energy into the two-particle vertex and allows to study the effects of quantum fluctuations beyond mean-field theory [9]. A crucial advantage of the PFFRG is that the diagrammatic summations include vertex corrections in all two-particle interaction channels, i.e., it treats magnetic ordering and disordering tendencies on an equal footing. Physical observables such as the momentum resolved DC magnetic susceptibility directly follow from the fermionic two-particle vertex. Most importantly, the FRG parameter Λ is proportional to the temperature T since both quantities act like an infrared frequency cutoff [11], Numerical benchmarks for an Ising model suggest that $T = \Lambda$ [12] which has also been used for the comparison of PFFRG and experimental data in Fig. **5c** of the main text. The evolution of the susceptibility as a function of Λ (i.e. T) enables us to probe the system with respect to magnetic order: a smooth divergence-free flow without signatures of an instability hints at a non-magnetic ground state, while a sharp cusp and breakdown of the Λ-flow indicates the onset of magnetic order. The momentum component at which this breakdown occurs further allows us to determine the wave vector of the magnetic order.

B. Stability of the disordered phase

As shown in Fig. **5** of the main text, the PFFRG method identifies a non-magnetic phase for an Hamiltonian with the exchange parameters of $Ca_{10}Cr_7O_{28}$ which were obtained in the previous section and are listed in equation (2). Here we discuss the stability of this phase when tuning the model parameters away from these values. To this end, we have performed additional PFFRG calculations along three line cuts in the parameter space. Starting from the exchange constants given in equation (2), we studied the following variations:

(i) $J0$ (bilayer coupling) is rescaled by a factor g_1 while the other couplings are kept constant

(ii) $J21$ and $J22$ (couplings of ferromagnetic triangles) are both rescaled by a factor g_2 while the other couplings are kept constant

(iii) $J31$ and $J32$ (couplings of antiferromagnetic triangles) are both rescaled by a factor g_3 while the other couplings are kept constant

In each case, the parameters g_1, g_2 or g_3 are tuned in the range $0.5, ..., 1.5$. Interestingly, the magnetic properties of the model turn out to be remarkably constant along all three line cuts. In Fig. **4**(a)-(c) we plot the momentum resolved static magnetic susceptibility for three representative cases on these lines. While the characteristic ring-like structure remains the same in all figures, the radius of the rings undergoes slight changes (note that Fig. **4**(b) shows the same result as Fig. **5d** in the main text). Small maxima marked by black dots are always found close to the position of 120° Néel order on a triangular superlattice. The positions of these maxima as a function

DOI: 10.1038/NPHYS3826

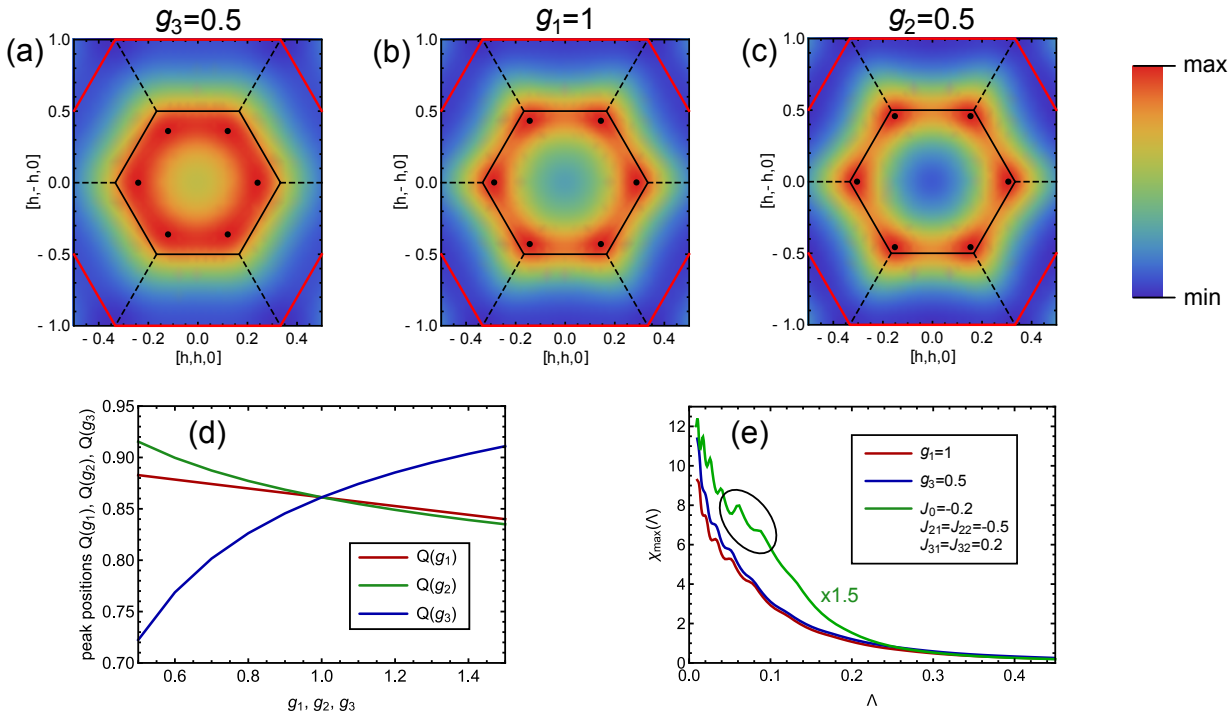

Figure 4. **PFFRG approach and the stability of the quantum disordered phase** (a) - (c) Momentum resolved profiles of the static magnetic susceptibility χ at $\Lambda = 0$. As in Fig. 5 in the main text, the black lines mark the boundaries of the first Brillouin zone while the red lines are the boundaries of the extended Brillouin zone. Black dots highlight the maximum positions of the susceptibility. Note that 120° Néel order corresponds to the corner position of the first Brillouin zone. (d) RG flows of the maximum of the susceptibility. The green curve has been multiplied by a factor of 1.5 for better visibility of all curves. An instability feature is marked by a black circle. For the red and blue line the largest exchange coupling $|J21|$ has been set to one, leading to dimensionless results for the susceptibility. (e) Distance of the peak positions from the center of the Brillouin zone for g_1, g_2, and g_3. The vertical axis is scaled such that $Q = 1$ corresponds to 120° Néel order on the triangular superlattice.

of g_1, g_2 and g_3 are plotted in Fig. **4**(d). As one would expect, increasing the ferromagnetic couplings (g1) and (g2) shifts the peaks further inside towards the center of the Brillouin zone while increasing the antiferromagnetic couplings (g3) shifts the peaks towards larger momenta. The strongest variation is observed when varying g_3.

Most importantly, the non-magnetic phase extends over almost the entire parameter regime. This is illustrated in Fig. **4**(e) showing the maximum of the susceptibility as a function of the frequency cutoff parameter Λ. Generally, in magnetically ordered systems the onset of a magnetic instability would manifest as a kink or a cusp in the Λ-flow (we plot the maximal susceptibility in momentum space since an instability would be most pronounced there). Apart from small oscillations at $\Lambda \lesssim 0.1$ which are unavoidable numerical artifacts due to the frequency discretization, the flows for $g_1 = 1$ and $g_3 = 0.5$ are very smooth and do not show any signatures of a magnetic instability. This type of flow behavior is characteristic for the whole parameter region that we studied. Only for small $g_2 \sim 0.5, ..., 0.6$ and large $g_3 \sim 1.5$ the system starts showing small indications for the onset of magnetic order which in total demonstrates the remarkable stability of the quantum disordered phase.

We emphasize, however, that the asymmetry of the couplings in both layers (i.e., the differences between $J21$ and $J22$ as well as between $J31$ and $J32$) significantly strengthens the quantum fluctuations. Setting $J21 = J22$ and $J31 = J32$ (e.g., by taking the respective mean values of our model parameters) quickly generates instability features in the RG flow showing the onset of magnetic order. An example for this type of flow behavior is plotted in Fig. **4**(e) (green line) where the susceptibility exhibits a kink at $\Lambda \approx 0.07$ (black circle).

The robustness of the non-magnetic phase is actually not surprising since a variation of the model parameters does not lead to a competition between different ordering tendencies. Increasing the ferromagnetic intralayer couplings $J21$ and $J22$ but leaving all other couplings fixed only generates a stronger binding of the spins $S = 1/2$ into spins $S = 3/2$. The main source of frustration arising from the interplay of ferromagnetic $J0$ and antiferromagnetic $J31$, $J32$ is, however, unaffected by this. On the other hand, decreasing the ferromagnetic intralayer couplings with respect to the other couplings weakens the stability of the effective spins $S = 3/2$. Such a reduction of ferromagnetic exchange increases the radius of the ring-like profile in the susceptibility. Only when the maximum in momentum space comes

close to the commensurate high symmetry point corresponding to 120° Néel state are quantum fluctuations reduced. This triggers the aforementioned small instability signatures at $g_2 \sim 0.5, ..., 0.6$ and $g_3 \sim 1.5$ and also leads to sharper peaks in the susceptibility, as shown in Fig. **4**(c). Once the spins are bound into effective spins $S = 3/2$ the frustration primarily results from the combination of ferromagnetic $J0$ and antiferromagnetic $J31$, $J32$. As long as the absolute values of these couplings are not too different, the system is fully frustrated and does not show any tendency towards magnetic order.

[1] Dalma Gyepesova and Vratislav Langer, "Ca10((CrO4)-O-V)(6)((CrO4)-O-VI), a disordered mixed-valence chromium compound exhibiting inversion twinning," Acta Cryst. **C69**, 111 (2013).

[2] C. Balz et al., to be published (2016).

[3] I. D. Brown and D. Altermatt, "Bond-valence parameters obtained from a systematic analysis of the Inorganic Crystal Structure Database," Acta Crystallographica Section B **41**, 244–247 (1985).

[4] R. D. Shannon, "Revised effective ionic radii and systematic studies of interatomic distances in halides and chalcogenides," Acta Crystallographica Section A **32**, 751–767 (1976).

[5] Iztok Arcon, Breda Mirtic, and Alojz Kodre, "Determination of valence states of chromium in calcium chromates by using x-ray absorption near-edge structure (xanes) spectroscopy," J. Am. Ceram. Soc. **81**, 222–224 (1998).

[6] R. Coldea, D. A. Tennant, K. Habicht, P. Smeibidl, C. Wolters, and Z. Tylczynski, "Direct measurement of the spin hamiltonian and observation of condensation of magnons in the 2d frustrated quantum magnet Cs_2CuCl_4," Phys. Rev. Lett. **88**, 137203 (2002).

[7] Kate A. Ross, Lucile Savary, Bruce D. Gaulin, and Leon Balents, "Quantum excitations in quantum spin ice," Phys. Rev. X **1**, 021002 (2011).

[8] S Toth and B Lake, "Linear spin wave theory for single-q incommensurate magnetic structures," Journal of Physics: Condensed Matter **27**, 166002 (2015).

[9] Johannes Reuther and Peter Wölfle, "J_1-J_2 frustrated two-dimensional heisenberg model: Random phase approximation and functional renormalization group," Phys. Rev. B **81**, 144410 (2010).

[10] A. A. Katanin, "Fulfillment of ward identities in the functional renormalization group approach," Phys. Rev. B **70**, 115109 (2004).

[11] Johannes Reuther, Ronny Thomale, and Simon Trebst, "Finite-temperature phase diagram of the heisenberg-kitaev model," Phys. Rev. B **84**, 100406 (2011).

[12] Stefan Göttel, Sabine Andergassen, Carsten Honerkamp, Dirk Schuricht, and Stefan Wessel, "Critical scales in anisotropic spin systems from functional renormalization," Phys. Rev. B **85**, 214406 (2012).